Mechanics of Materials 43 (2011) 349–360

Contents lists available at ScienceDirect

Mechanics of Materials

journal homepage: www.elsevier.com/locate/mechmat

Punch indentation of polyurea at different loading velocities: Experiments and numerical simulations

Jongmin Shim [a], Dirk Mohr [a,b,*]

[a] Impact and Crashworthiness Laboratory, Department of Mechanical Engineering, Massachusetts Institute of Technology, Cambridge, MA, USA
[b] Solid Mechanics Laboratory (CNRS-UMR 7649), Department of Mechanics, École Polytechnique, Palaiseau, France

ARTICLE INFO

Article history:
Received 29 October 2009
Received in revised form 17 November 2010
Available online 21 April 2011

Keywords:
Constitutive modeling
Finite strains
Non-linear viscoelasticity
Polyurea
Punch experiments
Time integration

ABSTRACT

Punch indentation experiments are performed on 10 mm thick polyurea layers on a steel substrate. A total of six different combinations of punch velocity, punch size and the lateral constraint conditions are considered. Furthermore, the time integration scheme for a newly-developed rate-dependent constitutive material model is presented and used to predict the force–displacement response for all experimental loading conditions. The comparison of the simulations and the experimental results reveals that the model is capable to predict the loading behavior with good accuracy for all experiments which is seen as a partial validation of the model assumptions regarding the pressure and rate sensitivity. As far as the unloading behavior is concerned, the model predicts the characteristic stiff and soft phases of unloading. However, the comparison of simulations and experiments also indicates that the overall model response is too stiff. The results from cyclic compression experiments suggest that the pronounced Mullins effect needs to be taken into account in future models for polyurea to improve the quantitative predictions during unloading.

1. Introduction

Polyurea is a highly viscoelastic rubber material that is used for the impact protection of vehicle structures. It is considered for the armor protection and retrofitting of military vehicles that are exposed to the blast loading of improvised explosive devices. The anticipated effect of polyurea coatings on the blast resistance of steel plates is twofold. Firstly, the polyurea can directly absorb a portion of the blast energy as it undergoes large deformations. Secondly, the onset of ductile fracture of a steel plate may be retarded through the use of a polyurea coating, thereby increasing the energy absorption of the steel structure. The amount of energy dissipation through polyurea coating is relating to the hysteresis area of the stress–strain curve under loading–unloading conditions. Recent experimental results (e.g. Ayoub et al., 2009) reported that some elastomers show asymmetric rate-sensitivity, i.e. strong rate-sensitivity during loading but weak rate-sensitivity during unloading. Thus, the proper prediction of unloading behavior is important to obtain a good estimation of the amount of energy dissipation.

As discussed by Xue and Hutchinson (2008), necking occurs under uniaxial tension when the average true stress becomes equal to the overall tangent hardening modulus (Considere criterion). In the case of a coated ductile substrate, a high strain hardening coating material can increase the effective hardening modulus of the bilayer material such that necking is retarded with respect to the Considere strain of the uncoated material. The bifurcation analysis of Guduru et al. (2006) reveals that an added surface layer can increase the resistance of a structural element to fragmentation. Moreover, their results show that the addition of a soft coating with high strain hardening can improve the weight specific energy absorption of the

* Corresponding author at: Impact and Crashworthiness Laboratory, Department of Mechanical Engineering, Massachusetts Institute of Technology, Cambridge, MA, USA.
E-mail address: mohr@mit.edu (D. Mohr).

0167-6636/$ - see front matter © 2011 Elsevier Ltd. All rights reserved.
doi:10.1016/j.mechmat.2011.04.001

structural element. Xue and Hutchinson (2008) demonstrate that the ratio of the elastomer modulus to the flow strength of the substrate controls the effect of necking retardation. McShane et al. (2008) performed tension and bulge tests on copper/polyurethane bilayers under static and dynamic conditions. Their experimental measurements indicate that coatings do not provide dynamic performance benefits on an equal mass basis. While the total blast resistance increases, the weight specific energy absorption of the structure may actually decrease through the application of a polymer coating. Dynamic ring expansion experiments have been performed by Zhang et al. (2009) on polyurea coated aluminum 6061-O and copper 101 at very high strain rates (4000–15,000/s). Their experimental results show that there is no significant effect of the polyurea coating on the strain at the onset of localization.

It appears that the neck retardation effect in coated ductile substrates is difficult to achieve when using polyurea in combination with typical engineering materials. However, as pointed out by McShane et al. (2008), polyurea coatings may still be seen as a practical solution for enhancing the blast resistance of metallic structures because of the ease of applying polyurea on existing structures (retrofitting). Even though the performance of the steel substrate may remain unaffected, a very thick polyurea layer can still increase the energy absorption in absolute terms. The impulsive loading experiments of Amini et al. (2010c) reveal that polyurea coatings have a strong effect on the energy transfer to the steel plate. In particular, they demonstrate that the positioning of polyurea on the impact side promotes failure of the steel plate under shock loading while a polyurea layer on the back of the plate attenuates the shock. In the present paper, we deal with the prediction of the large deformation behavior of polyurea in structural applications. Xue and Hutchinson (2008) made use of a Moonley–Rivlin model for the polymer coating in their numerical analysis of the polymer/metal bilayers. Zhang et al. (2009) modeled the behavior of polyurea using a non-linear hyperelastic material model. However, both uniaxial compression and tension tests have demonstrated that the mechanical response of polyurea is highly strain-rate dependent (e.g. Amirkhizi et al., 2006; Roland et al., 2007; Sarva et al., 2007; Shim and Mohr, 2009). Amini et al. (2010d) make use of the temperature-, rate- and pressure-sensitive constitutive model by Amirkhizi et al. (2006) to provide supporting simulation results of their direct pressure pulse experiments. They also recently reported the effect of asymmetric tension–compression response and the hydrostatic pressure on the blast resistance of polyurea/steel plates (Amini et al., 2010a, 2010b).

Finite viscoelasticity models of elastomers may be formulated using the so-called hereditary integral approach (Coleman and Noll, 1961; Bernstein et al., 1963; Lianis, 1963; McGuirt and Lianis, 1970; Leonov, 1976; Johnson et al., 1994; Haupt and Lion, 2002; Amirkhizi et al., 2006) but their validity is often limited to a narrow range of strain rates (Yang et al., 2000; Shim et al., 2004; Hoo Fatt and Ouyang, 2007). As an alternative to the hereditary integral approach, the framework of multiplicative decomposition of the deformation gradient (Kröner, 1960; Lee, 1969) is frequently used in finite viscoelasticity (e.g. Sidoroff, 1974; Lubliner, 1985; Le Tallec et al., 1993; Reese and Govindjee, 1998; Huber and Tsakmakis, 2000). In that framework, the non-linear viscoelasticity of elastomers is commonly described through a rheological spring-dashpot models of the Zener type (e.g. Roland, 1989; Johnson et al., 1995; Bergström and Boyce, 1998; Huber and Tsakmakis, 2000; Quintavalla and Johnson, 2004; Bergström and Hilbert, 2005; Qi and Boyce, 2005; Areias and Matous, 2008; Hoo Fatt and Ouyang, 2008; Tomita et al., 2008).

For the coating applications to blast and ballistic mitigations, the hydrostatic pressure and temperature as well as strain rates play a critical role to determine the mechanical properties of the polyurea under the loading. It is known that two different types of viscoelastic behavial modes are observed in polymeric materials including polyurea: global chain mode responsible for rubbery and flow properties and local segmental mode responsible for behavior below glass transition temperature (e.g. Roland and Casalini, 2007). The temperature–pressure dependences are strongly influenced by those viscoelastic modes, however, very limited experimental studies have been reported on the effect of pressure and temperature (Amirkhizi et al., 2006; Roland and Casalini, 2007; Roland et al., 2010). Although the universal constitutive model for polyurea should include all the effects, the proposed model in the paper, as the first engineering approach, considers only the effect of strain rates for the rubbery viscoelastic behavior. In the present work, we present the time integration scheme for a newly developed rate-dependent constitutive model for polyurea (Shim and Mohr, 2011). After implementing the model as a user material subroutine into a commercial finite element software, the model is used to predict the mechanical response of thick polyurea layers under punch loading. Experiments are performed on 10 mm thick polyurea layers for different punch velocities and different hemispherical punch radii. It is found that the model provides an accurate description of the loading phase, which validates the assumptions made with respect to strain-rate and pressure sensitivity. However, the predicted response deviates from the experimental result during unloading which is discussed in detail.

2. Punch experiments

2.1. Specimens

The polyurea specimens used in the study are extracted from a 5 mm thick steel armor plate with a 12.7 mm thick layer of polyurea DragonShield-HT Explosive Resistant Coating (ERC). Rectangular samples of 46×40 mm are cut from the coated armor plate using conventional machining. The coated polyurea is not separated from the steel as the steel substrate serves as specimen support throughout the punching experiments. However, to guarantee a uniform layer thickness for all specimens, the thickness of the polyurea layer is reduced to 10 mm though conventional machining (milling at room

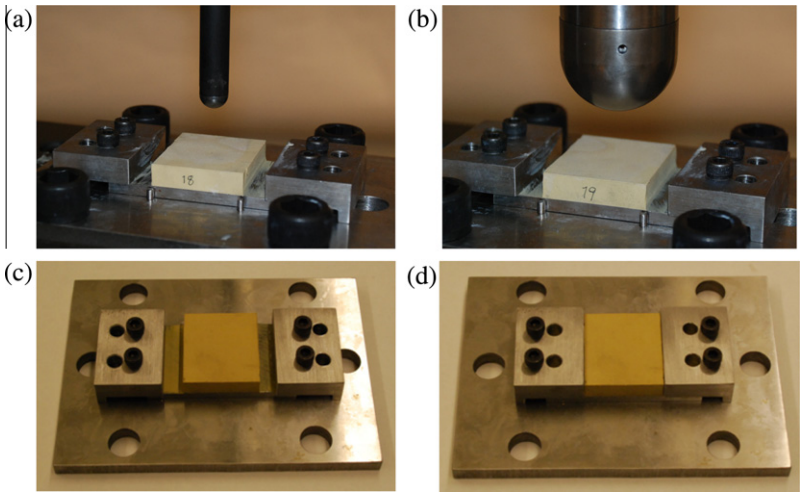

Fig. 1. Photos of the experiments with (a) the small punch and (b) the large punch. The second row shows the set up for (c) free boundaries in all lateral directions and (d) for constrained boundary conditions in the width direction.

temperature). All experiments are performed on polyurea in its virgin state (no prior loading) after a shelf life of about four years.

2.2. Experimental procedure

The specimens are clamped on the table of a hydraulic testing machine (Model 8080, Instron). The specimens are loaded through hemispherical indenters that are attached to the moving actuator of the upper crosshead. Two hemispherical indenters of different sizes are employed: $D = 12.7$ mm (Fig. 1a) and $D = 44.45$ mm (Fig. 1b). In addition, we consider two different types of lateral boundary conditions: (1) free in all lateral directions (Fig. 1c), and (2) constrained in the width direction (Fig. 1d). For the latter case, the polyurea specimen is placed between two steel blocks which prevents bulging in the width direction, but does not prevent possible shrinking of the specimen in width direction. The friction at the interface between the indenters and the polyurea is reduced by grease and multiple 0.1 mm thick Teflon layers (which are partially torn apart during the test). The experiments are performed under displacement control at constant deceleration using the control software MAX (Instron, Canton). Starting with an initial velocity v_0, the velocity-time profile decreases linearly until the experiment is stopped at a velocity of $-v_0$ (Fig. 2a). The initial position of the actuator is chosen such that the loading direction is reversed (point $v = 0$) when the punch depth reaches 7 mm (Fig. 2b). Experiments are performed for $v_0 = 1$ mm/s and $v_0 = 100$ mm/s. Throughout all experiments, the punch force is measured using a 50 kN load cell. The punch displacement is measured using an LVDT that is integrated in the actuator. The overall stiffness of the testing frame is about 100 kN/mm (Shim and Mohr, 2009). All displacements reported in the following have been corrected by the deformation associated with the finite machine stiffness.

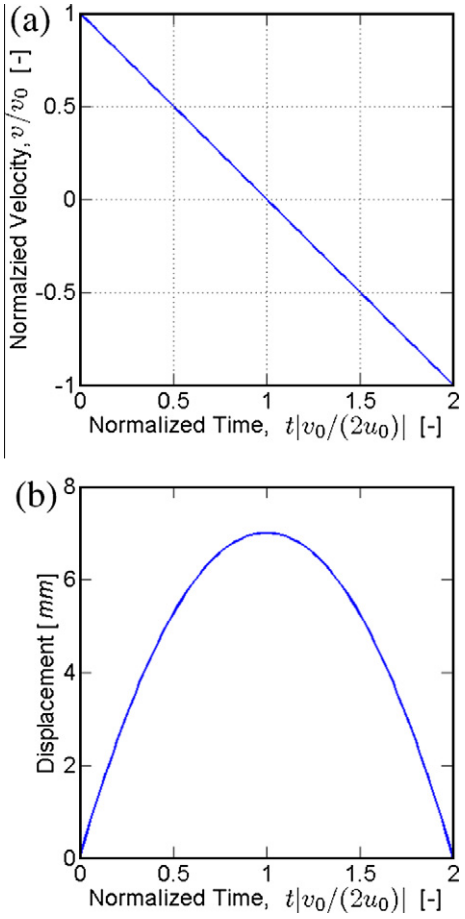

Fig. 2. Applied loading profiles: (a) Applied velocity history; the velocity axis is normalized by the applied initial velocity of either $v_0 = 1$ or 100 mm/s; the time axis is normalized by $|2u_0/v_0|$ with $u_0 = 7$ mm; (b) Corresponding applied displacement history.

2.3. Experimental results

Fig. 3a summarizes the results for the experiments with the small hemispherical indenter (D = 12.7 mm). The measured force–displacement curves are monotonically increasing up to the point of load reversal. During unloading, the force reaches zero at a displacement of about 3.2 mm. Beyond that point, the punch moves faster than the surface of the creeping polyurea specimen. The force level is about 40% higher in a punch test at v_0 = 100 mm/s than at v_0 = 1 mm/s which is mostly due to the rate dependent material behavior. Note that the loading conditions are of quasi-static nature since the speed of elastic waves in polyurea is much faster (of the order of 10^6 mm/s) than the loading velocities. It is interesting to observe the convergence of the force–displacement curves for both velocities upon unloading which is consistent with the results from uniaxial compression experiments (Shim and Mohr, 2011). The results with and without constraint in the width direction are almost identical. For clarity, Fig. 3a presents the results for free lateral boundary conditions only.

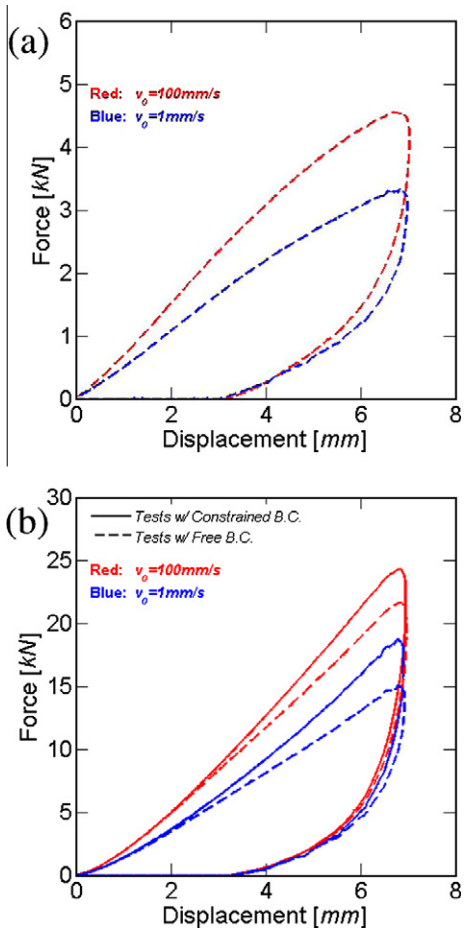

Fig. 3. Measured load–displacement curves for experiments with (a) the small punch, (b) the large punch.

In close analogy with the results from the small punch experiments, the measured force–displacement curves for the large hemispherical punch experiments (see Fig. 3b) are loading velocity sensitive and display a higher force level for the higher loading velocity. Moreover, the large punch experiments also show the characteristic convergence of the force–displacement curves during unloading. For the large punch, the force level is zero at a punch displacement of 3.4 mm. The effect of the boundary condition in width direction becomes apparent when using the large hemispherical punch (D = 44.45 mm): the force level with the constraint (solid lines) is higher than that with the free lateral boundary conditions (dotted lines). Regardless of the applied velocity profiles, the constraint in the width direction increases the force level by about 3 kN at the maximum punching depth. The effect of strain rate yields an increase of the force level of up to 7 kN when changing the loading velocity from v_0 = 1 mm/s to v_0 = 100 mm/s.

3. Constitutive model

In the following, we present the algorithmic version of a recently-developed constitutive model for polyurea. The reader is referred to Shim and Mohr (2011) for details on the differential formulation and the underlying physical arguments for specific constitutive equations. The algorithm is implemented as a user material subroutine for the finite element software Abaqus/explicit. In order to describe the viscoelastic behavior of elastomers, some researchers adopted Zener-type models, which are composed of a spring (rate-independent part for average stress–strain behavior) in parallel with a Maxwell element (rate-dependent part). However, due to the strong asymmetric rate-sensitivity of polyurea, the concept of equilibrium path (represented by the average stress-strain behavior) breaks down in the case of polyurea. Consequently, conventional Zener-type models are not suitable for the modeling of the viscoelastic response of polyurea. Here, the proposed constitutive equations are based on a rheological model of two Maxwell elements that act in parallel (Fig. 4). The first Maxwell element represents the soft part (Network A) of polyurea and is composed of a non-linear viscous damper and a non-linear Gent spring. The hard part (Network B) is represented by another non-linear viscous damper and a Hencky spring. The equations are cast in a framework of finite strains with multiplicative Kröner–Lee decomposition (Kröner, 1960; Lee, 1969) of

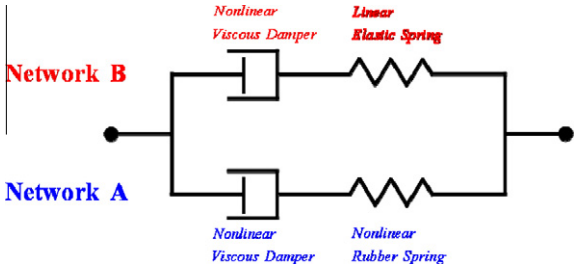

Fig. 4. Rheological model of the rate dependent constitutive model for polyurea.

the deformation gradient for each Maxwell element. The specific evolution laws for individual model components are given in algorithmic form below. The Euler forward numerical integration method is employed within the subroutine, because of numerical challenges associated with Euler backward integration schemes for Maxwell models with non-linear rubber springs and non-linear dashpots (e.g. Areias and Matous, 2008).

In the material model, the macroscopic deformation gradient $\mathbf{F}_{tot}$ is decomposed into a volumetric part $\mathbf{F}_{vol}$,

$$\mathbf{F}_{vol} = J^{1/3}\mathbf{1} \quad \text{with} \quad J = \det \mathbf{F}_{tot} \tag{1}$$

and an isochoric part $\mathbf{F}$,

$$\mathbf{F} = J^{-1/3}\mathbf{F}_{tot}. \tag{2}$$

The isochoric deformation gradients within both networks, $\mathbf{F}_A$ and $\mathbf{F}_B$ equal the macroscopic isochoric deformation gradient

$$\mathbf{F} = \mathbf{F}_A = \mathbf{F}_B. \tag{3}$$

For a Maxwell element K, the isochoric deformation gradient can be multiplicatively decomposed into an elastic part $\mathbf{F}_K^e$ and viscous part $\mathbf{F}_K^v$

$$\mathbf{F}_K = \mathbf{F}_K^e\mathbf{F}_K^v \quad \text{where} \quad K = A, B. \tag{4}$$

The material model comprises the viscous deformation gradients of Networks A and B, $\mathbf{F}_A^v$ and $\mathbf{F}_B^v$, as internal state variables. We consider the strain driven time integration problem, where the variables at time $\tau = t + \Delta t$ are calculated based on the solution at time t. In other words, given the total deformation gradient $\mathbf{F}_{tot}(\tau)$ and the internal state variables $\mathbf{F}_A^v(t)$ and $\mathbf{F}_B^v(t)$, we evaluate the total Cauchy stress $\mathbf{T}(\tau)$ along with the updated state variables $\mathbf{F}_A^v(\tau)$ and $\mathbf{F}_B^v(\tau)$. The hydrostatic part of the Cauchy stress tensor is directly related to the change in total volume,

$$J(\tau) = \det \mathbf{F}_{tot}(\tau), \tag{5}$$

$$\frac{\mathrm{tr}\mathbf{T}(\tau)}{3} = \kappa\frac{\ln J(\tau)}{J(\tau)}, \tag{6}$$

with κ denoting the bulk modulus. The deviatoric part of the macroscopic stress tensor corresponds to the sum of the deviatoric stresses $\mathbf{T}_A$ and $\mathbf{T}_B$ acting on Networks A and B, respectively,

$$\begin{aligned}\mathbf{T}(\tau) &= \mathrm{dev}\{\mathbf{T}(\tau)\} + \frac{\mathrm{tr}\mathbf{T}(\tau)}{3}\mathbf{1} \\ &= \mathbf{T}_A(\tau) + \mathbf{T}_B(\tau) + \frac{\mathrm{tr}\mathbf{T}(\tau)}{3}\mathbf{1}.\end{aligned} \tag{7}$$

Table 1
Summary of material parameters identified from monotonic loading–unloading experiments at five different strain rates.

Isochoric part of Network A	Gent spring	μ_A	7.00 MPa
		J_A	10.7
	Dashpot A	P_A	4.42 MPa
		n_A	0.0646
Isochoric part of Network B	Hencky spring	μ_B	82.3 MPa
	Dashpot B	Q_B	0.0447
		n_B	0.0755
Volumetric part		κ	829 MPa

For the evaluation of the stresses and internal variables in Networks A and B, it is useful to define the isochoric deformation gradient

$$\mathbf{F}(\tau) = [J(\tau)]^{-1/3}\mathbf{F}_{tot}(\tau) \tag{8}$$

as well as the strain-like deformation measure

$$\zeta(\tau) = \sqrt{\mathrm{tr}\{\mathbf{F}^T(\tau)\mathbf{F}(\tau)\} - 3}. \tag{9}$$

3.1. Response of Network A

The viscous deformation gradient $\mathbf{F}_A^v(\tau)$ is approximated by the Euler forward form

$$\mathbf{F}_A^v(\tau) = [\mathbf{1} + \Delta t\mathbf{L}_A^v(t)]\mathbf{F}_A^v(t), \tag{10}$$

where $\mathbf{L}_A^v(t)$ is the rate of viscous deformation at time t, and it is assumed to be spin-free, i.e. $\mathbf{L}_A^v(t) := \mathbf{D}_A^v(t)$. Subsequently, we calculate the isochoric deformation gradient of the elastic deformation in Network A,

$$\mathbf{F}_A^e(\tau) = \mathbf{F}_A(\tau)[\mathbf{F}_A^v(\tau)]^{-1}. \tag{11}$$

Using $\mathbf{F}_A^e(\tau)$, we determine the deviatoric Cauchy stress for Network A based on Gent's (1996) free energy function

$$\mathbf{T}_A(\tau) = \frac{\mu_A}{J(\tau)}\left(1 - \frac{\mathrm{tr}\{\mathbf{F}_A^{eT}(\tau)\mathbf{F}_A^e(\tau)\} - 3}{J_A}\right)^{-1}\mathrm{dev}\{\mathbf{F}_A^e(\tau)\mathbf{F}_A^{eT}(\tau)\}, \tag{12}$$

with the material parameters $\mu_A > 0$ (initial modulus) and $J_A > 1$ (locking stretch).

The viscous rate of deformation tensor $\mathbf{D}_A^v(\tau)$ is obtained from the non-linear viscous evolution law. For this, we calculate the driving Mandel stress

$$\mathbf{M}_A(\tau) = J(\tau)\,\mathrm{dev}\{\mathbf{F}_A^{eT}(\tau)\mathbf{T}_A(\tau)\mathbf{F}_A^{e-T}(\tau)\}, \tag{13}$$

along with the corresponding equivalent stress

$$\bar{m}_A(\tau) = \sqrt{\frac{3}{2}\mathbf{M}_A(\tau) : \mathbf{M}_A(\tau)}. \tag{14}$$

The equivalent rate of viscous deformation $\bar{d}_A(\tau)$ is then given by the power-law

$$\bar{d}_A(\tau) = d_0\left\langle\frac{\bar{m}_A(\tau)}{P_A[\exp\zeta(\tau) - 1]}\right\rangle^{1/n_A} \tag{15}$$

with the reference rate of deformation $d_0 = 1/s$ and the material properties $P_A > 0$ (viscosity constant) and the exponent $n_A > 0$. The flow rule assumes that the rate of viscous deformation tensor $\mathbf{D}_A^v$ is aligned with the driving Mandel stress $\mathbf{M}_A$,

$$\mathbf{D}_A^v(\tau) = \frac{3}{2}\frac{\bar{d}_A(\tau)}{\bar{m}_A(\tau)}\mathbf{M}_A(\tau). \tag{16}$$

3.2. Response of Network B

In close analogy with the procedure for Network A, the constitutive equations for Network B are solved numerically. We assume

$$\mathbf{F}_B^{v}(\tau) = [\mathbf{1} + \Delta t\, \mathbf{D}_B^{v}(t)]\mathbf{F}_B^{v}(t) \tag{17}$$

and

$$\mathbf{F}_B^{e}(\tau) = \mathbf{F}_B(\tau)[\mathbf{F}_B^{v}(\tau)]^{-1}. \tag{18}$$

The stiff elastic response of Network B is described by Hencky's strain energy function. Thus, elastic right stretch tensor $\mathbf{U}_B^e(\tau)$ and the rotation tensor $\mathbf{R}_B^e(\tau)$ are calculated from the polar decomposition of the elastic deformation gradient,

$$\mathbf{F}_B^{e}(\tau) = \mathbf{R}_B^{e}(\tau)\mathbf{U}_B^{e}(\tau) \quad \text{with} \quad \mathbf{R}_B^{eT}(\tau)\mathbf{R}_B^{e}(\tau) = \mathbf{1} \tag{19}$$

before calculating the deviatoric Cauchy stress

$$\mathbf{T}_B(\tau) = \frac{2\mu_B}{J(\tau)}\mathbf{R}_B^{e}(\tau)[\ln \mathbf{U}_B^{e}(\tau)]\mathbf{R}_B^{eT}(\tau) \tag{20}$$

with the shear modulus $\mu_B > 0$ (initial modulus). Subsequently, we write

$$\mathbf{M}_B(\tau) = J(\tau)\mathrm{dev}\left\{\mathbf{F}_B^{eT}(\tau)\mathbf{T}_B(\tau)\mathbf{F}_B^{e-T}(\tau)\right\} \tag{21}$$

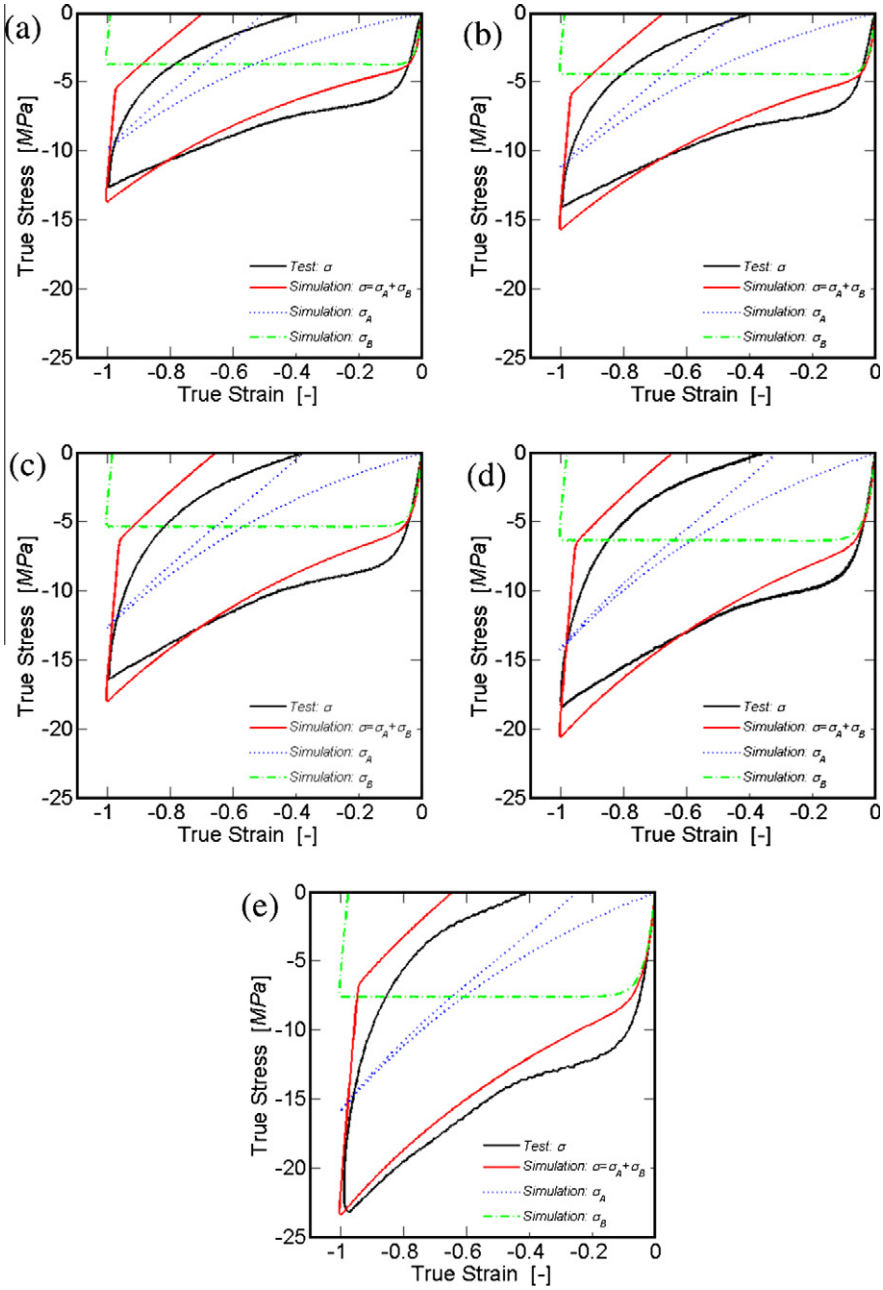

Fig. 5. Comparison of simulation results and experiments for continuous loading–unloading cycles. (a) $\dot{\varepsilon} = 10^{-3}$/s, (b) $\dot{\varepsilon} = 10^{-2}$/s, (c) $\dot{\varepsilon} = 10^{-1}$/s, (d) $\dot{\varepsilon} = 10^{0}$/s, (e) $\dot{\varepsilon} = 10^{1}$/s (reproduced from Shim and Mohr (2011)).

and

$$\bar{m}_B(\tau) = \sqrt{\frac{3}{2}\mathbf{M}_B(\tau) : \mathbf{M}_B(\tau)}. \tag{22}$$

The rate of viscous deformation $\bar{d}_B(\tau)$ is approximated by

$$\bar{d}_B(\tau) = d_0 \left\langle \frac{\bar{m}_B(\tau)}{\sqrt{3}\mu_B Q_B} \left\{ 1 - \exp\left[-\frac{\zeta(\tau)}{Q_B} \left(\frac{\bar{d}_B(t)}{d_0} \right)^{-n_B} \right] \right\}^{-1} \right\rangle^{1/n_B}, \tag{23}$$

where $Q_B > 0$ and $n_B > 0$ are material model parameters that control the rate sensitivity of Network B. As for Network A, the rate of viscous deformation tensor $\mathbf{D}_B^v$ is aligned with the driving Mandel stress $\mathbf{M}_B$,

$$\mathbf{D}_B^v(\tau) = \frac{3}{2}\frac{\bar{d}_B(\tau)}{\bar{m}_B(\tau)}\mathbf{M}_B(\tau). \tag{24}$$

3.3. Model parameter identification

The constitutive model requires the identification of eight material parameters: four parameters (μ_A, J_A, P_A, n_A) for Network A, three parameters (μ_B, Q_B, n_B) for Network B, and one parameter (κ) describing the elastic volumetric response. All model parameters have been identified based on the results from uniaxial compression experiments at five different strain rates between 10^{-3}/s and 10^{1}/s up to a true strain of -1.0. Digital image correlation has been used to measure both the axial and transverse strains. Details on the parameter identification procedure are given in Shim and Mohr (2011). Table 1 summarizes the identified material parameters which are used in the present structural validation study. The comparison of the measured and predicted stress–strain curves for uniaxial compression is shown in Fig. 5. It is noted that the present choice of material model parameters provides a good description of the monotonic loading response of polyurea, while the model predictions are systematically too stiff during unloading.

4. Numerical simulations of the punch experiments

Finite element simulations are performed of all punch experiments. We make use of the symmetry of the mechanical system by using a quarter model. The polyurea block is meshed with eight-node reduced integration solid elements (type C3D8R of the Abaqus element library) while using the user material option is used to describe the constitutive behavior. The punches are modeled using rigid elements. The meshes comprise eight elements in thickness direction and a small geometric bias in the horizontal plane with a smaller element size near the center than at the specimen boundaries. Frictionless interface conditions are assumed between the punch and the polyurea. The motion of all nodes at the bottom of the polyurea (which corresponds to the interface with the steel substrate in the experiment) is set to zero. We applied the same punch velocity histories as in the experiments and omitted the addition of bulk viscosity.

The deformed meshes at the point of maximum penetration ($u = 7$ mm) are shown in Fig. 6 for the simulation

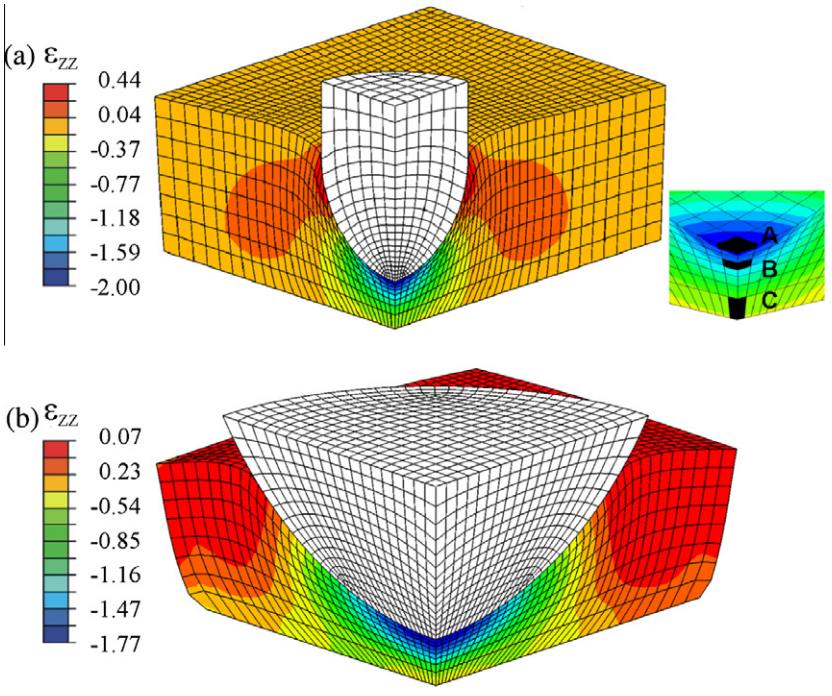

Fig. 6. The contour plots of the logarithmic strain in thickness-direction from simulations with $v_0 = 100$ mm/s at an indentation depth of 7 mm: (a) small hemispherical indenter, and (b) large hemispherical indenter. The detail in Fig. 6a shows the locations for which the strain rates $\bar{d}_A$ and $\bar{d}_B$ are plotted in Fig. 8.

without lateral constraint along the width direction. The comparison of Figs. 6a and b clearly shows that the bulging effect; observe that the lateral expansion of the polyurea block is more pronounced for the large than for the small punch. In the latter case, we observe a small lateral displacement of 0.5 mm. The bulging has little effect on the load–displacement curves for the small punch and we found nearly the same force–displacement curve for free and constrained lateral boundary conditions.

The predicted force–displacement curves for the small punch are shown in Fig. 7a. The simulations results are in good agreement with the measured force–displacement curves during the loading phase. A similar conclusion may be drawn from comparing the simulations and experiments for the large punch (Figs. 7b and c). The comparison shows that the numerical model can predict (a) the effect of the punch size, (b) the effect of the lateral boundary constraint, and (c) the effect of loading velocity on the force–displacement curve during loading. Fig. 8 shows the histories of the strain-like variable, ζ, and the viscous rates, $\bar{d}_A$ and $\bar{d}_B$, for the simulation of a small punch with $v_0 = 100$ mm/s (the corresponding locations are highlighted in Fig. 6a). The profiles elucidate the strong variations in local viscous strain rate during the punch experiments. It is interesting to see that the local viscous strain rate can be as high as 30/s which is close to the strain rate of the fastest calibration experiment (Fig. 5e). However, unlike for the calibration experiments, the strain rates are non-constant throughout a punch tests which is seen as an important validation of the model assumptions with respect to the effect of strain rate. At a punching depth of 7 mm, the simulation results overestimate the force level by about 0.5 kN in the case of the small punch (Fig. 7a) and 2.5 kN in the case of the large punch (Figs. 7b and c). This overestimation (which corresponds to less than 10% of the current force level) is consistent with the model calibration results. Recall from Fig. 5 that the model systematically overestimates the stress level at very large compressive strains.

The model predictions during unloading deviate from the experimentally-measured force–displacement responses. The simulations predict the characteristic convergence of the load–displacement curves, but the predicted response during unloading is too stiff for both velocities and both punch sizes. Consequently, the instantaneous residual displacement at zero force is overestimated in the simulations. This deviation is again consistent with the calibration experiments, indicating an inherent shortcoming of the model formulation for unloading.

5. Discussion

The loading response of the model agrees well with the test results except for an overestimation of the force at

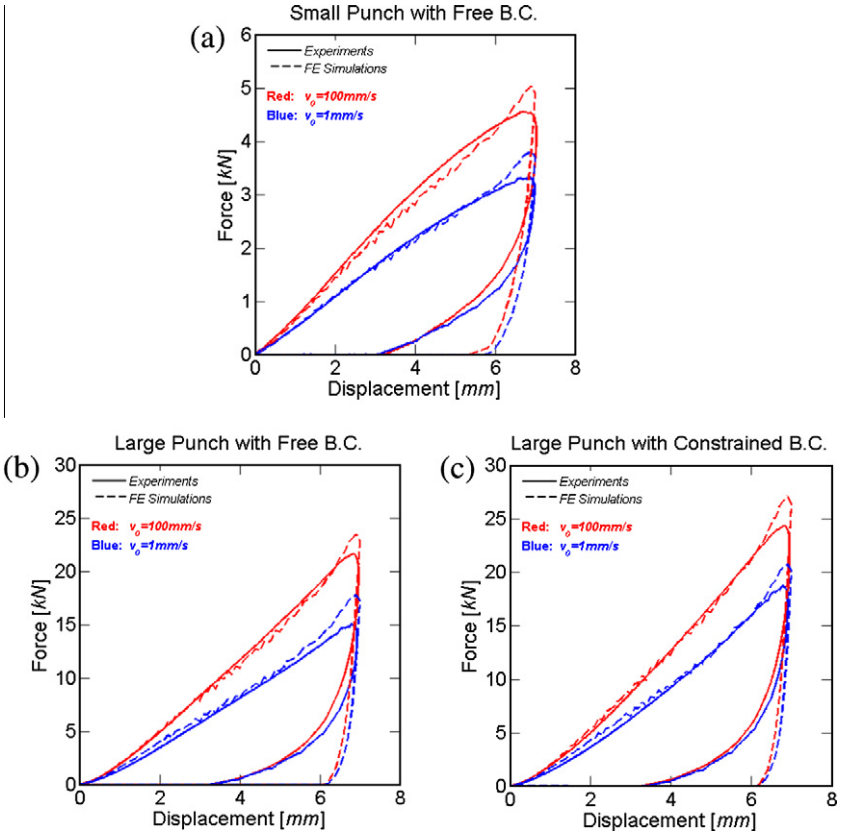

Fig. 7. Comparison of simulations and experiments. Force–displacement curves for (a) small punch with free lateral boundaries, (b) large punch with the free lateral boundaries, (c) large punch with constraint in the width direction.

large punch displacements. However, during unloading, the model overestimates the stiffness. The simulation results indicate that the material is subject to strains of up to −2.0 as the punching depth reaches 7 mm (see Fig. 6). Since this is twice as high as in the experiments for the material model parameter identification, we performed additional material tests at a strain rate of 10^{-2}/s. Fig. 9a shows the resulting stress–strain curve from three different experiments. Each virgin-state specimen is subject to a single loading–unloading cycle up to a maximum strain of −0.5, −1.0 and −1.5, respectively. The corresponding simulations (Fig. 9b) reveal that the numerically-predicted locking behavior is more severe than that observed in the experiments.

The unloading path in the stress–strain curves comprises two characteristic regimes: a stiff part at the beginning of unloading followed by a soft part as the stress approaches zero. Both the experiments and the numerical simulations exhibit this feature. The numerical model does not show the smooth transition between these two regimes, but this is seen as an acceptable engineering approximation of the physical behavior. However, the apparent main deficiency of the current model is its inability to capture the increase of the hysteresis loop width as the strain increases. As the applied maximum strain increases, the simulations predict almost constant stress drops (marked by a′, b′, and c′ in Fig. 9b) while the experiments show a substantial increase in the magnitude of the stress drops as a function of strain (marked by a, b, and c in Fig. 9a).

Recall that Network A in the current constitutive model is mainly responsible for the rubbery behavior while Network B describes the high initial stiffness and the time-dependent hysteresis. The contributions of Networks A and B are in opposite direction as far as the hysteresis width is concerned. To shed more light on this particular feature, Fig. 10 shows a direct comparison of the model response and the experiments. In addition, we plotted the individual contributions of Networks A and B to the stress–strain curve (dashed curves in Fig. 10). Note that the magnitude of the stress contribution of Network B depends on the compressive strain only, while its sign changes from compression to tension upon unloading. The contribution of Network A on the other hand is a compressive stress irrespective of the loading direction. Thus, as the compressive strain increases, Network B makes the hysteresis wider while the opposite holds true for Network A. In order to replicate the experimental observation of a

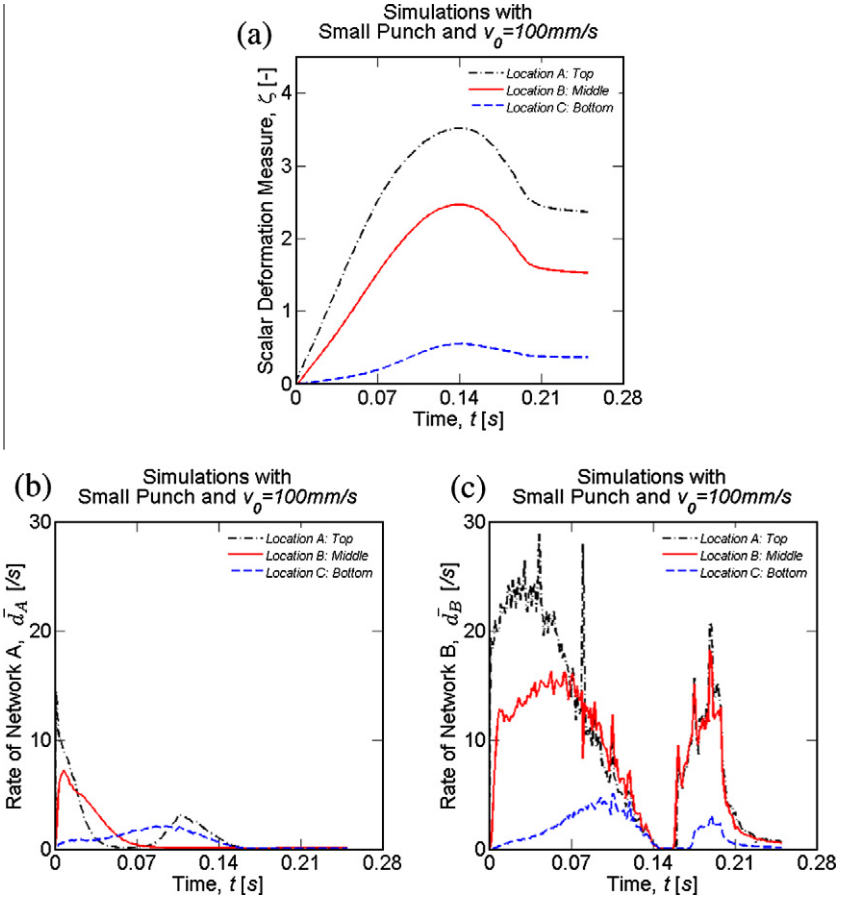

Fig. 8. Results from the small punch simulation with v_0 = 100 mm/s and free lateral boundary conditions at three different locations (labeled by A, B and C in Fig. 6a): histories of (a) the strain-like deformation measure ζ, (b) the viscous strain rate of network A, $\bar{d}_A$, (c) the viscous strain rate of network B, $\bar{d}_B$. Note that the loading direction is reversed at t = 0.14 s.

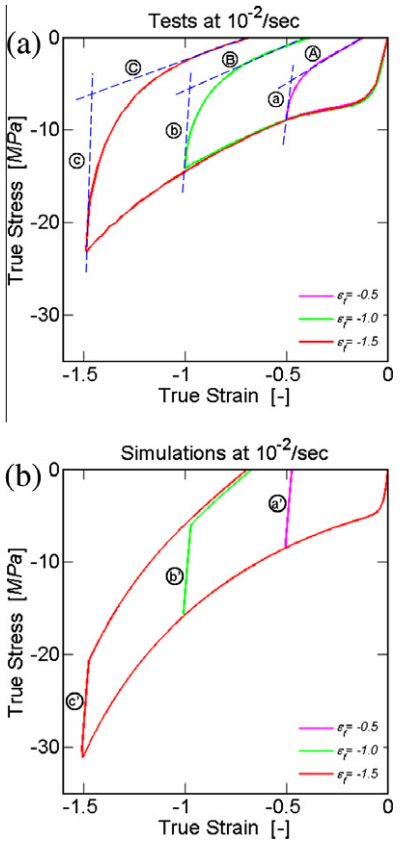

Fig. 9. Stress–strain curves for a single loading–unloading cycle at $\dot{\varepsilon} = 10^{-2}$/s as obtained from (a) experiments and (b) simulations.

hysteresis width increase as a function of the maximum compressive strain (Fig. 9a), the contribution of Network B should be dominant. Moreover, the contribution of Network B would need to increase as the compressive strain increases. However, due to the specific choice of the viscous evolution law for Network B, the stress contribution of Network B is more or less constant once the compressive strain has exceeded −0.1 (see the stress plateau in the response curves for Network B in Fig. 10). An attempt was made to change the calibration of the response of Network B using the present modeling framework, but the subsequent simulation results were no longer satisfactory for the phase of loading.

A constitutive model with a different rheological composition needs to be used to improve the predictions for unloading. A previous study (Shim and Mohr, 2011) has shown that models of the Zener-type (spring in parallel with a single Maxwell element) cannot describe the large deformation behavior of polyurea over a wide range of strain rates. The present results indicate that the assumption of two Maxwell elements in parallel provides an accurate description for monotonic loading only. It can describe the two characteristic stiff and soft regimes during unloading over a wide range of strain rates, but the model predictions are only in poor quantitative agreement during unloading.

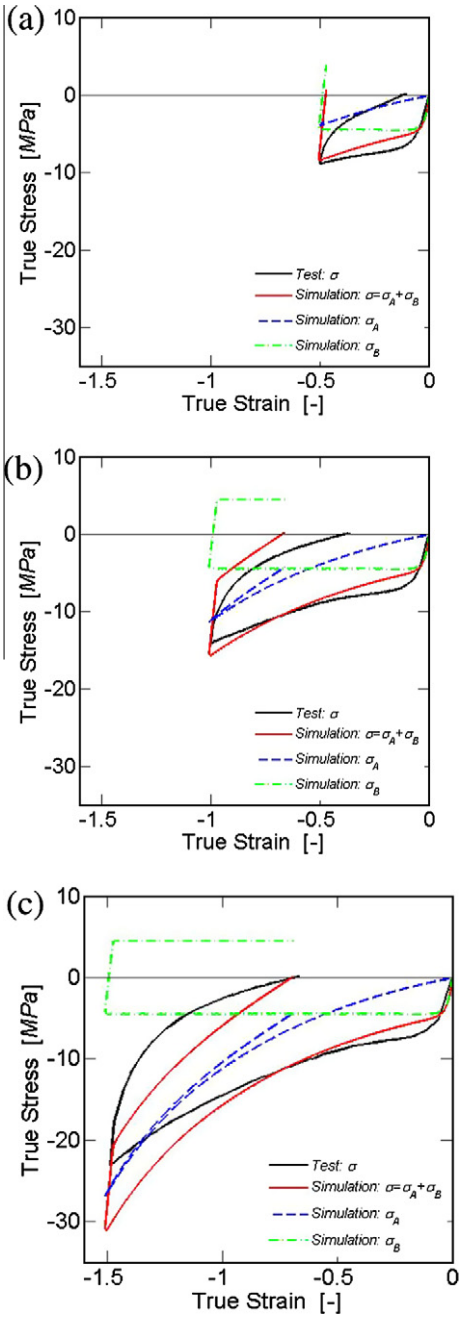

Fig. 10. Comparison of simulation results and experiments for loading–unloading cycles at $\dot{\varepsilon} = 10^{-2}$/s. (a) $\varepsilon_f = -0.5$, (b) $\varepsilon_f = -1.0$, (c) $\varepsilon_f = -1.5$.

Throughout our model development, we focused on a single loading–unloading cycle on virgin-state specimens. However, even though the loading of the material in its virgin state appears to be the most important with respect to the real-life applications of polyurea, the material response to cyclic loading may be instructive as far as the choice of the rheological model is concerned. Fig. 11 shows the stress–strain curve for polyurea for five consecutive loading–unloading cycles. After each loading–unloading cycle at a constant true strain rate of 10^{-2}/s, we let the specimen

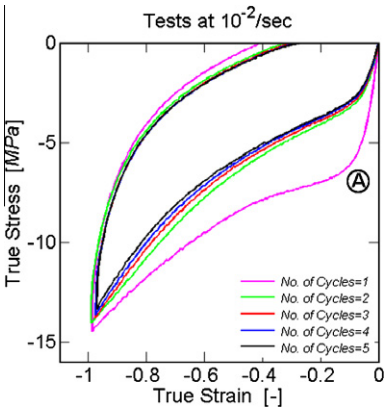

Fig. 11. Illustration of the Mullins effect. Five compression loading and unlading cycles are performed at the constant strain rate of 10^{-2}/s up to the maximum strain of -1.0. The stress is zero between subsequent cycles for about 5 min.

creep at zero stress for about 300 s before applying the subsequent loading–unloading cycle. The significant difference between the first and subsequent loading cycles illustrates the Mullins effect for polyurea. The stress–strain curve for the first loading is characterized by the high initial stiffness and the high peak stress marked as A. After the first loading–unloading cycle, however, the shape of the loading path changes noticeably while nearly the same unloading path is observed. Additional loading–unloading cycles create very little changes in both loading and unloading. This observation suggests that the constitutive model should comprise an internal variable that reflects the amount of "microstructural damage" associated with the Mullins effect. The Mullins effect has been investigated by many research groups using either damage-based constitutive models (e.g. Simo, 1987; Govindjee and Simo, 1991, 1992; Lion, 1996, 1997; Miehe and Keck, 2000) or the concept of hard/soft domain reorganization (e.g. Johnson and Beatty, 1993a, 1993b; Beatty and Krishnaswamy, 2000; Qi and Boyce, 2004, 2005). Here, the explicit account of the Mullins effect is deferred to future work since further experimental data is needed to analyze the effect of loading velocity over a wide range of strain rates.

6. Conclusion

Punch experiments have been performed on 10 mm thick polyurea samples at punch velocities of up to 100 mm/s which resulted in maximum local viscous strain rates of up to 30/s inside the polyurea layers. A newly-developed rate-dependent constitutive model for polyurea has been implemented into a finite element program and used to predict the experimentally-measured force–displacement curves for different punch sizes and velocities. Furthermore, the effect of lateral constraints has been investigated. The model provides accurate predictions of the loading response for all six test configurations which is interpreted as a partial validation of the assumptions made with respect to strain-rate and pressure sensitivity. During unloading, the model exhibits the characteristic stiff and soft responses of polyurea; however, it systematically overestimates the depth of the quasi-instantaneous residual punch imprint after unloading.

Acknowledgement

Thanks are due to Professor Tomasz Wierzbicki from MIT for valuable discussions. The partial financial support through the Office of Naval Research (ONR) Grant # N00014-07-1-0821 and the French National Center for Scientific Research (CNRS) is gratefully acknowledged.

References

Amini, M.R., Amirkhizi, A.V., Nemat-Nasser, S., 2010a. Numerical modeling of response of monolithic and bilayer plates to impulsive loads. International Journal of Impact Engineering 37, 90–102.

Amini, M.R., Isaacs, J.B., Nemat-Nasser, S., 2010b. Experimental investigation of response of monolithic and bilayer plates to impulsive loads. International Journal of Impact Engineering 37, 82–89.

Amini, M.R., Simon, J., Nemat-Nasser, S., 2010c. Numerical modeling of effect of polyurea on response of steel plates to impulsive loads in direct pressure–pulse experiments. Mechanics of Materials 42, 615–627.

Amini, M.R., Isaacs, J., Nemat-Nasser, S., 2010d. Investigation of effect of polyurea on response of steel plates to impulsive loads in direct pressure–pulse experiments. Mechanics of Materials 42, 628–639.

Amirkhizi, A.V., Isaacs, J., McGee, J., Nemat-Nasser, S., 2006. An experimentally-based viscoelastic constitutive model for polyurea, including pressure and temperature effects. Philosophical Magazine 86, 5847–5866.

Areias, P., Matous, K., 2008. Finite element formulation for modeling nonlinear viscoelastic elastomers. Computational Methods in Applied Mechanical Engineering 197, 4702–4717.

Ayouba, G., Zaïria, F., Naït-Abdelaziza, M., Gloaguenb, J.M., 2009. Modelling large deformation behaviour under loading–unloading of semicrystalline polymers: Application to a high density polyethylene. International Journal of Plasticity 26 (3), 329–347.

Bergström, J.S., Boyce, M.C., 1998. Constitutive modeling of the large strain time-dependent behavior of elastomers. Journal of the Mechanics and Physics of Solids 46, 931–954.

Bergström, J.S., Hilbert, L.B., 2005. A constitutive model of predicting the large deformation thermomechanical behavior of fluoropolymers. Mechanics of Materials 37, 899–913.

Bernstein, B., Kersley, E.A., Zapas, L.J., 1963. A study of stress relaxation with finite strain. Transaction of the Society of Rheology 7, 391–410.

Beatty, M.F., Krishnaswamy, S., 2000. A theory of stress-softening in incompressible isotropic materials. Journal of the Mechanics and Physics of Solids 48, 1931–1965.

Coleman, B.D., Noll, W., 1961. Foundations of linear viscosity. Reviews of Modern Physics 33, 239–249.

Gent, A.N., 1996. A new constitutive relation for rubber. Rubber Chemistry and Technology 69, 59–61.

Govindjee, S., Simo, J., 1991. A micro-mechanically based continuum damage model for carbon black-filled rubbers incorporating Mullins effect. Journal of the Mechanics and Physics of Solids 39, 87–112.

Govindjee, S., Simo, J., 1992. Mullins effect and the strain amplitude dependence of the storage modulus. International Journal of Solids and Structures 29, 1737–1751.

Guduru, P.R., Bharath, M.S., Freund, L.B., 2006. The influence of a surface coating on the high-rate fragmentation of a ductile material. International Journal of Fracture 137, 89–108.

Haupt, P., Lion, A., 2002. On finite linear viscoelasticity of incompressible isotropic materials. Acta Mechanica 159, 87–124.

Hoo Fatt, M.S., Ouyang, X., 2007. Integral-based constitutive equation for rubber at high strain rates. International Journal of Solids and Structures 44, 6491–6506.

Hoo Fatt, M.S., Ouyang, X., 2008. Three-dimensional constitutive equations for styrene butadiene rubber at high strain rates. Mechanics of Materials 40, 1–16.

Huber, N., Tsakmakis, C., 2000. Finite deformation viscoelasticity laws. Mechanics of Materials 32, 1–18.

Johnson, A.R., Quigley, C.J., Freese, C.E., 1995. A visco hyperelastic finite element model for rubber. Computational Methods in Applied Mechanical Engineering 127, 163–180.

Johnson, A.R., Quigley, C.J., Mead, J.L., 1994. Large-strain viscoelastic constitutive models for rubber. I. Formulations. Rubber Chemistry and Technology 67, 904–917.

Johnson, M.A., Beatty, M.F., 1993a. The Mullins effect in uniaxial extension and its influence on the transverse vibration of a rubber string. Continuum Mechanics and Thermodynamics 5, 83–115.

Johnson, M.A., Beatty, M.F., 1993b. A constitutive equation for the Mullins effect in stress controlled uniaxial extension experiments. Continuum Mechanics and Thermodynamics 5, 301–318.

Kröner, E., 1960. Allgemeine kontinuumstheorie der versetzungen und eigenspannungen. Archive for Rational Mechanics and Analysis 4, 273–334.

Lee, E.H., 1969. Elastic plastic deformation at finite strain. ASME Journal of Applied Mechanics 36, 1–6.

Leonov, A.I., 1976. Nonequilibrium thermodynamics and rheology of viscoelastic polymer media. Rheologica Acta 15, 85–98.

Le Tallec, P., Rahier, C., Kaiss, A., 1993. Three-dimensional incompressible viscoelasticity in large strains: formulation and numerical approximation. Computer Methods in Applied Mechanics and Engineering 109, 233–258.

Lianis, G., 1963. Constitutive Equations of Viscoelastic Solids under Large Deformations. A & ES Report No. 63-5, Purdue University.

Lion, A., 1996. A constitutive model for carbon black filled rubber: experimental investigations and mathematical representation. Continuum Mechanics and Thermodynamics 8, 153–169.

Lion, A., 1997. A physically based method to represent the thermo-mechanical behaviour of elastomers. Acta Mechanica 123, 1–25.

Lubliner, J., 1985. A model of rubber viscoelasticity. Mechanics Research Communications 12, 93–99.

McGuirt, C.W., Lianis, G., 1970. Constitutive equations for viscoelastic solids under finite uniaxial and biaxial deformations. Transaction of the Society of Rheology 14, 117–134.

McShane, G.J., Stewart, C., Aronson, M.T., Wadley, H.N.G., Fleck, N.A., Deshpande, V.S., 2008. Dynamic rupture of polymer-metal bilayer plates. International Journal of Solids and Structures 45, 4407–4426.

Miehe, C., Keck, J., 2000. Superimposed finite elastic–viscoelastic–plastoelastic stress response with damage in filled rubbery polymers. Experiments, modelling and algorithmic implementation. Journal of the Mechanics and Physics of Solids 48, 323–365.

Qi, H.J., Boyce, M.C., 2004. Constitutive model for stretch-induced softening of the stress–stretch behavior of elastomeric materials. Journal of the Mechanics and Physics of Solids 52, 2187–2205.

Qi, H.J., Boyce, M.C., 2005. Stress–strain behavior of thermoplastic polyurethanes. Mechanics of Materials 37, 817–839.

Quintavalla, S.J., Johnson, S.H., 2004. Extension of the Bergstrom–Boyce model to high strain rates. Rubber Chemistry and Technology 77, 972–981.

Reese, S., Govindjee, S., 1998. A theory of finite viscoelasticity and numerical aspects. International Journal of Solids and Structures 35, 3455–3482.

Roland, C.M., 1989. Network recovery from uniaxial extension. I: Elastic equilibrium. Rubber Chemistry Technology 62, 863–879.

Roland, C.M., Casalini, R., 2007. Effect of hydrostatic pressure on the viscoelastic response of polyurea. Polymer 48, 5747–5752.

Roland, C.M., Fragiadakis, D., Gamache, R.M., 2010. Elastomer–steel laminate armor. Composite Structures 92, 1059–1064.

Roland, C.M., Twigg, J.N., Vu, Y., Mott, P.H., 2007. High strain rate mechanical behavior of polyurea. Polymer 48, 574–578.

Sarva, S.S., Deschanel, S., Boyce, M.C., Chen, W., 2007. Stress–strain behavior of a polyurea and a polyurethane from low to high strain rates. Polymer 48, 2208–2213.

Shim, J., Mohr, D., 2009. Using split Hopkinson pressure bars to perform large strain compression tests on polyurea at low, intermediate and high strain rates. International Journal of Impact Engineering 36, 1116–1127.

Shim, J., Mohr, D., 2011. Finite strain constitutive model of polyurea for a wide range of strain rates. International Journal of Plasticity 27.

Shim, V.P.W., Yang, L.M., Lim, C.T., Law, P.H., 2004. A visco-hyperelastic constitutive model to characterize both tensile and compressive behavior of rubber. Journal of Applied Polymer Science 92, 523–531.

Sidoroff, F., 1974. Un modèle viscoélastique non linéaire avec configuration intermédiaire. Journal de Mécanique 13, 679–713.

Simo, J.C., 1987. On a fully 3-dimensional finite-strain viscoelastic damage model – formulation and computational aspects. Computer Methods in Applied Mechanics and Engineering 60, 153–173.

Tomita, Y., Azuma, K., Naito, M., 2008. Computational evaluation of strain-rate-dependent deformation behavior of rubber and carbon-black-filled rubber under monotonic and cyclic straining. International Journal of Mechanical Sciences 50, 856–868.

Yang, L.M., Shim, V.P.W., Lim, C.T., 2000. A visco-hyperelastic approach to modelling the constitutive behaviour of rubber. International Journal of Impact Engineering 24, 545–560.

Xue, Z.Y., Hutchinson, J.W., 2008. Neck development in metal/elastomer bilayers under dynamic stretchings. International Journal of Solids and Structures 45, 3769–3778.

Zhang, H., Liechti, K.M., Ravi-Chandar, K., 2009. On the dynamics of localization and fragmentation-III. Effect of cladding with a polymer. International Journal of Fracture 155, 101–118.